AIP | Journal of Applied Physics

One-dimensional time-dependent fluid model of a very high density low-pressure inductively coupled plasma

Vernon H. Chaplin and Paul M. Bellan

Citation: Journal of Applied Physics **118**, 243303 (2015); doi: 10.1063/1.4938490
View online: http://dx.doi.org/10.1063/1.4938490
View Table of Contents: http://scitation.aip.org/content/aip/journal/jap/118/24?ver=pdfcov
Published by the AIP Publishing

One-dimensional time-dependent fluid model of a very high density low-pressure inductively coupled plasma

Vernon H. Chaplin and Paul M. Bellan
Applied Physics Department, California Institute of Technology, Pasadena, California 91125, USA

(Received 22 August 2015; accepted 10 December 2015; published online 28 December 2015)

A time-dependent two-fluid model has been developed to understand axial variations in the plasma parameters in a very high density (peak $n_e \gtrsim 5 \times 10^{19}\,\mathrm{m}^{-3}$) argon inductively coupled discharge in a long 1.1 cm radius tube. The model equations are written in 1D with radial losses to the tube walls accounted for by the inclusion of effective particle and energy sink terms. The ambipolar diffusion equation and electron energy equation are solved to find the electron density $n_e(z,t)$ and temperature $T_e(z,t)$, and the populations of the neutral argon 4*s* metastable, 4*s* resonant, and 4*p* excited state manifolds are calculated to determine the stepwise ionization rate and calculate radiative energy losses. The model has been validated through comparisons with Langmuir probe ion saturation current measurements; close agreement between the simulated and measured axial plasma density profiles and the initial density rise rate at each location was obtained at $p_{Ar} = 30 - 60\,\mathrm{mTorr}$. We present detailed results from calculations at 60 mTorr, including the time-dependent electron temperature, excited state populations, and energy budget within and downstream of the radiofrequency antenna. © *2015 AIP Publishing LLC*. [http://dx.doi.org/10.1063/1.4938490]

I. INTRODUCTION

Low-pressure ($\lesssim$1 Torr) radiofrequency (RF) inductively coupled plasmas (ICPs) are widely used in integrated circuit fabrication and other materials processing,[1,2] and significant effort has been devoted to numerically modeling their behavior. Global (zero-dimensional) models[3,4] that solve for the volume-averaged electron density (n_e) and temperature (T_e) have proven to be quite useful for estimating the steady-state or time-dependent plasma parameters, while complex two-dimensional (2D)[5,6] and 3D[7] fluid and hybrid models have been constructed to make detailed predictions about the spatial variations of these parameters. The various types of models produce qualitatively similar conclusions about the basic discharge properties and time evolution: for example, T_e is expected to decay much more quickly than n_e in the afterglow of a pulsed discharge.[2] Generally, one would like to construct the simplest model that adequately captures the processes of interest; the improvement in accuracy that is gained through additional complexity must be weighed against increased computational time and the risk of obscuring intuition about the fundamental driving mechanisms for the observed behavior. Simulations that can run rapidly on a personal computer (PC) are particularly useful for plasma source design[8] and for efficiently investigating a range of possible discharge operating regimes.

In this paper, we describe a two-fluid model for a high density ($n_e > 10^{19}\,\mathrm{m}^{-3}$) pulsed argon ICP in a high aspect ratio cylindrical discharge tube. A RF plasma source was used for pre-ionization in the Caltech Magnetohydrodynamically (MHD)-Driven Jet Experiment (see Fig. 1(a)), a pulsed power experiment that simulates astrophysical accretion disk jets.[9] RF plasma was created in a quartz tube behind the jet experiment electrodes and then expanded into a larger vacuum chamber. The main goal of modeling was to predict the time-dependent plasma density downstream of the source at the entrance to the main chamber; the extent to which the plasma parameters varied in the radial direction was of less importance to the success of the experiment. Therefore a time-dependent 1D transport model was developed.

Although the model equations were solved in the axial direction only, it was critical to accurately account for losses of charged particles and energy to the tube walls as the plasma flowed away from the antenna. We follow the approach taken by many global models[3,4] and calculate the loss rate using a well-known steady-state radial diffusion solution, so our model is in fact quasi-2D. This is in contrast to a previous 1D ICP model developed by Lymberopoulos *et al.*[11] that assumed an infinite slab geometry. Henriques *et al.*[12] constructed a 1D steady-state model of a surface wave-heated discharge in which radial losses were accounted for using an approach similar to ours, but they did not solve any transport equations in the axial direction; instead, axial gradients in the plasma parameters arose solely due to spatial variations in the deposited wave power.

Models of "high-density" ICPs for plasma processing have typically considered densities in the range $10^{17} - 10^{18}\,\mathrm{m}^{-3}$,[2–4,6] but peak densities in our RF discharge were one to two orders of magnitude higher than this. In this very high density regime, which has seldom been modeled, stepwise ionization dominates over direct ionization from the ground state,[4,10] so tracking excited level populations is important. We approximate neutral argon's complex atomic structure using a five-level atom[3,4] in which the two 4s resonant, two 4s metastable, and ten 4p levels are each grouped together, and highly excited states above the 4*p* level are neglected. The model also accounts for the effect of radiation trapping on the effective spontaneous transition rates.

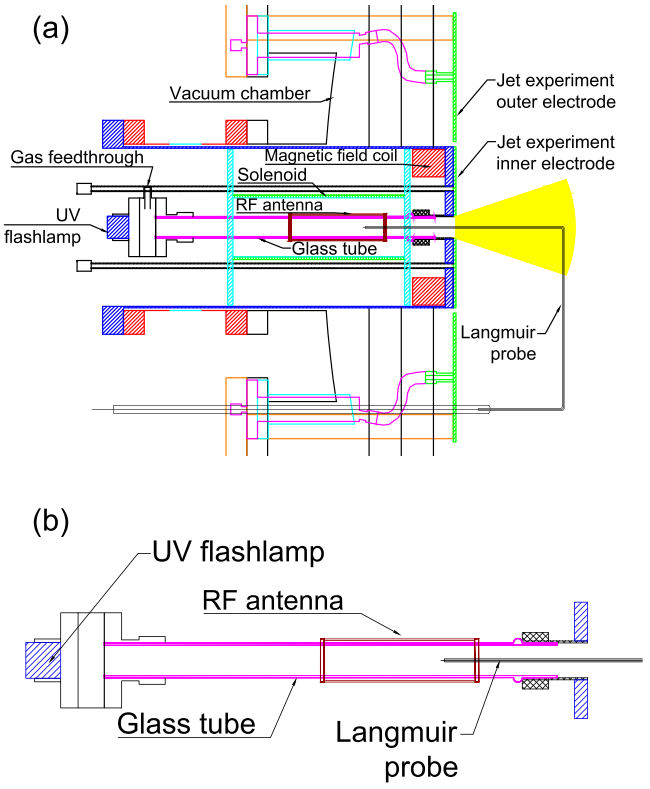

FIG. 1. (a) Side-on cross-sectional view of the RF discharge tube and coaxial electrodes on the Caltech MHD-Driven Jet Experiment. Adapted from Ref. 10. The cable leading to the RF antenna and some other minor hardware elements have been omitted for clarity. As illustrated in the figure, plasma created inside the antenna expanded into the main vacuum chamber where it was used to seed ionization of additional neutral gas in the pulsed power experiment. (b) Close-up of the cylindrical discharge tube—understanding the RF plasma transport inside the tube is the focus of this paper.

Our 1D model is fully self-consistent and has only two free parameters: the fraction of the total RF power delivered to the load that is absorbed by the plasma and the ion temperature T_i, which is assumed to be constant and equal to the neutral gas temperature T_g. The approximations in the model derivation (see Sec. III C) are expected to be valid for gas pressures $p_{Ar} \geq 30$ mTorr, and the best agreement between the computational results and the experimental data was obtained at 30–60 mTorr (see Sec. IV A). In this regime, the model can provide detailed insights into the discharge physics that cannot easily be obtained from experimental measurements.

II. EXPERIMENT

Details of the experiment setup and motivation have been described previously,[10] and only a brief overview of the portion of the apparatus relevant to the modeling work will be given here. A custom battery-powered 3 kW 13.56 MHz RF amplifier was used to drive a 10.5 cm long half-turn helical antenna[13] surrounding the $R = 1.1$ cm inner radius quartz tube shown in Fig. 1, creating a high-density plasma that expanded away from the antenna in both directions. In the usual configuration, the nearest end of the antenna was located 5.9 cm behind the plane of the jet experiment electrodes, which we define to be at $z = 0$ cm. The RF amplifier was pulsed for 0.1–1 ms, and a xenon arc UV flashlamp (Excelitas Technologies model FX-1165) was triggered at the time of RF turn-on to provide seed ionization and improve the reproducibility of the discharge. For MHD-driven jet experiments, argon gas was transiently injected at the rear end of the discharge tube using a fast pulsed gas valve; however, this procedure led to an unknown nonuniform pressure distribution in the tube, hindering quantitative comparisons between the data and computational model results, so a uniform argon backfill of $30\,\text{mTorr} \leq p_{Ar} \leq 300\,\text{mTorr}$ was used in experiments to validate the model. In some experiments, a background magnetic field was applied using the coil and solenoid shown in Fig. 1(a), but only the unmagnetized case will be considered in this paper.

The RF discharge properties were diagnosed using a cylindrical single Langmuir probe with exposed surface area $A = 4.5 \times 10^{-6}\,\text{m}^2$ that entered the discharge tube from the main chamber and could move along the tube axis, as shown in Fig. 1. When the RF amplifier was operated at full power, typical plasma densities inside the antenna were $n_i \approx n_e \sim 5 \times 10^{19}\,\text{m}^{-3}$ or higher. It was originally expected that a high downstream density in front of the jet experiment electrodes would only be obtained when an axial magnetic field was applied to reduce radial losses; however, early experiments revealed that $n_e > 10^{18}\,\text{m}^{-3}$ could be achieved beyond the end of the quartz tube even with $B = 0$. This observation prompted a modeling effort to understand the balance of ionization, transport, and loss processes in the tube.

III. DESCRIPTION OF THE MODEL

A. Simulation domain and boundary conditions

The computational domain for the 1D model is illustrated in Fig. 2. We approximate the experiment (shown in Fig. 1(b)) as a long uniform radius discharge tube (the plasma expansion into the larger chamber at the right-hand side of Fig. 1(a) will not be analyzed) with the RF antenna located near the center of the domain. The tube length in the model is chosen to be $L = 1$ m, much longer than the region of interest for the experiment, so that zero density and zero heat flux boundary conditions can be applied at the ends. We assume that RF power is deposited uniformly within an 9.5 cm-long region inside the antenna with no power absorbed elsewhere. A simpler assumption would be to set the length of the power absorption region equal to the antenna length (10.5 cm); however, Langmuir probe data (see Figs. 5–7) showed a delay of several μs between the initial density rise at $z = -7$ cm and the time at which the density began to rise at $z = -6$ cm, implying that plasma had to be transported to $z = -6$ cm rather than being created there initially.

B. Atomic processes

The atomic processes included in the model are illustrated in Fig. 3. The subscripts g, m, r, and p refer to the neutral argon (Ar I) ground state, 4s metastable state, 4s resonant state, and 4p state, respectively, and i refers to the

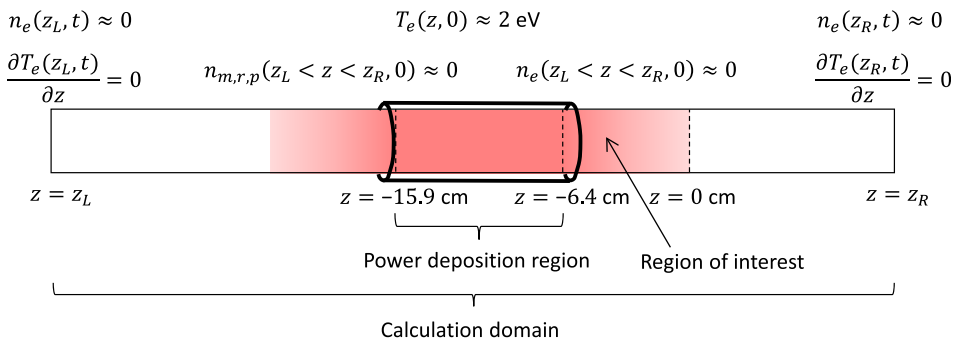

FIG. 2. Illustration of the simulation domain, boundary conditions, and initial conditions. The jet experiment electrodes were located at $z = 0$ cm, and the main goal of the model was to understand the transport and atomic processes at $-7\,\text{cm} < z < 0\,\text{cm}$. A low, non-zero density was specified at the boundaries in order to maintain numerical stability. No boundary conditions were necessary for the excited state population densities n_m, n_r, and n_p because there are no spatial derivatives in Eqs. (23)–(25).

ionized state (Ar II). Ar II excited states and multiply charged ions are neglected; this is a reasonable approximation because the ionization fraction is <10% at the power levels and pressures of interest. Formulas for the rate coefficients for collisional processes as a function of T_e are taken from Lieberman and Lichtenberg (Ref. 1, Table 3.3). The electron velocity distribution is assumed to be Maxwellian.

Three-body recombination is of negligible importance while the RF power is on, but it is included to more accurately model the afterglow period. The recombination rate per unit volume is approximately $K_{rec.}n_e^3$, where the rate coefficient[14] in m^6/s is

$$K_{rec.} \approx \frac{C' E_{gi}^{7/2}}{7\eta^{7/2} k_B^{7/2} T_e^{9/2}}, \tag{1}$$

where $C' = 6.74 \times 10^{-38}\,\text{m}^6\,\text{K}\,\text{s}^{-1}$. η is a dimensionless number that parameterizes the position of the "bottleneck" energy level below which spontaneous transitions begin to dominate over collisional de-excitation as electrons cascade to the ground state following recombination. Its value has been estimated to be between 1 and 4 by different authors;[14] we adopt the value $\eta = 2$. Recombination occurs most frequently into highly excited states,[14] so we assume that all recombinations occur into the $4p$ state (which is the highest Ar I energy level in our model) with each recombination transferring an energy $E_{pi} = 1.53\,\text{eV}$ to the free electrons. This would be an excellent approximation of reality if the true bottleneck level was at or below the $4p$ level because the cascade of collisional de-excitations following recombination would ultimately lead to an equivalent 1.53 eV of energy transfer to the free electrons. However, the bottleneck state is expected to be higher than the $4p$ level, so our treatment of recombination overestimates the reheating of the electrons to some extent. Fortunately, the contribution of recombination to the overall energy budget is small—see Fig. 11.

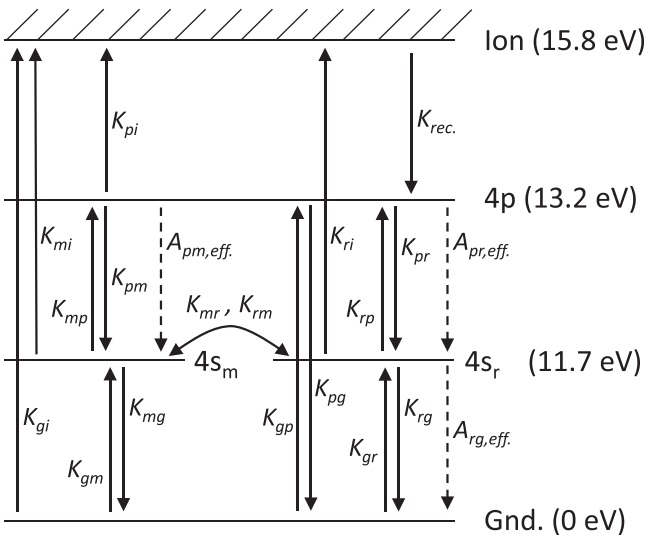

FIG. 3. Ar I energy level structure (not to scale) and collisional and radiative transitions included in the model. Solid arrows indicate electron-impact excitations and de-excitations with rate coefficients $K_{\alpha\beta}$ and three-body recombination with rate coefficient $K_{rec.}$, while dotted lines indicate spontaneous transitions with absorption-corrected transition rates $A_{\alpha\beta,eff.}$. Adapted from Ref. 10.

The rates $A_{\alpha\beta}$ for spontaneous radiative transitions from level α to level β[15] are corrected for the effect of reabsorption within the discharge tube by following an approximate procedure developed by Ashida *et al.*[3] All photons emitted at a distance $d > l_{mfp}$ from the tube walls are assumed to be re-absorbed, while those emitted within one absorption mean free path l_{mfp} of the boundary escape. Thus when $l_{mfp} = (n_\beta \sigma_{\lambda_0})^{-1}$ is smaller than the tube radius R, the effective transition rate is given by

$$A_{\alpha\beta,eff.}(z,t) = A_{\alpha\beta}\left(\frac{\pi R^2 - \pi(R - l_{mfp}(z,t))^2}{\pi R^2}\right). \tag{2}$$

The line center absorption cross section (including the effect of stimulated emission) for a Doppler-broadened emission line[16] is

$$\sigma_{\lambda_0} = \frac{\lambda_0^3}{8\sqrt{2}\pi^{3/2}} \frac{g_\alpha}{g_\beta} A_{\alpha\beta}\left(1 - \frac{g_\beta n_\alpha}{g_\alpha n_\beta}\right)\sqrt{\frac{M}{k_B T_g}}, \tag{3}$$

where $M = 6.7 \times 10^{-26}\,\text{kg}$ for argon. The overall effective transition rates out of the $4s$ resonant and $4p$ manifolds are determined by first calculating $A_{\alpha\beta,eff}$ for each individual spontaneous transition depopulating a $4s$ resonant or $4p$ level and then taking a weighted average of these (for example,

$A_{pm,eff.} = \sum g_\alpha A_{\alpha m,eff.}/g_p$, where g_α are the upper level statistical weights for individual transitions and $g_p = 36$ is the total statistical weight of the $4p$ manifold). For more details, see Ref. 17, Appendix E.

C. Model equations

The starting point for the model is the standard two-fluid equations for plasmas (Ref. 18, Sec. 2.5), including the electron and ion continuity and momentum equations and the electron energy equation. The ion and neutral temperatures will be treated as a free parameter $T_i = T_g$, assumed to be constant, so that we may avoid solving the ion and neutral energy equations. The electron temperature and the Ar I excited state population densities are assumed to be uniform in the radial direction but can vary axially. We assume a parabolic radial plasma density profile, $n_e(r,z) = n_{e,central}(z)(1 - r^2/R^2)$, which closely approximates the radial profiles obtained in detailed two-dimensional calculations for the relevant pressure regime by other authors.[19,20] This profile function will not appear explicitly in the 1D model, but it determines the ratio of the on-axis density $n_{e,central}$ to the density averaged over the plasma cross section, which is the quantity that appears in the equations. Specifically,

$$\langle n_e \rangle = \frac{1}{\pi R^2}\int_0^{2\pi}\int_0^R n_{e,central}\left(1 - \frac{r^2}{R^2}\right) r dr d\phi = \frac{1}{2} n_{e,central}. \quad (4)$$

To determine which terms in the two-fluid equations may be safely neglected, we will estimate the magnitude of each term by assuming that the characteristic length scale for the problem is $l_{char.} = 5\,\text{cm}$, the characteristic time scale is $t_{char.} = 20\,\mu\text{s}$ (so $f_{char.} = 50\,\text{kHz}$ and $\omega_{char.} \approx 3 \times 10^5\,\text{rad./s}$), the characteristic temperatures are $T_{e,char.} = 2\,\text{eV}$ and $T_{i,char.} = 0.05\,\text{eV}$, and the pressure is $p_{Ar} = 100\,\text{mTorr}$ (so the density of neutral atoms plus ions is $n_{total} = 3.33 \times 10^{21}\,\text{m}^{-3}$).

The ratio of the inertial term to the collisional drag term in the momentum equation is

$$\frac{|n_\sigma m_\sigma \frac{d\mathbf{u}_\sigma}{dt}|}{|\nu_{\sigma n} m_\sigma n_\sigma \mathbf{u}_\sigma|} \sim \frac{\omega_{char.}}{\nu_{\sigma n}} = \frac{\omega_{char.}}{n_g \sigma_{\sigma n} v_{T\sigma}}, \quad (5)$$

where the subscript σ represents either electrons or ions and $\nu_{\sigma n}$ is the collision frequency. Collisions are assumed to occur with low-velocity neutral atoms; electron-ion collisions are unimportant because quasineutrality requires that the two charged species move together with the same mean fluid velocity $\mathbf{u}_e = \mathbf{u}_i \equiv \mathbf{u}$. The cross sections are $\sigma_{en} \approx 5 \times 10^{-20}\,\text{m}^2$ and $\sigma_{in} \approx 5 \times 10^{-19}\,\text{m}^2$ (Ref. 1, Figs. 3.13 and 3.15), so using the characteristic parameters defined above, we find $\omega_{char.}/\nu_{en} \approx 2 \times 10^{-3}$ and $\omega_{char.}/\nu_{in} \approx 0.37$. Thus the inertial term in the electron momentum equation is negligible and can be dropped. Following the standard approach for deriving ambipolar diffusion (Ref. 1, Sec. 5.1), we will also neglect the inertial term in the ion momentum equation even though its magnitude is within a factor of 3 of the magnitude of the collisional term for the assumed discharge parameters. This approximation will limit the ability of the model to capture high-frequency phenomena. With the magnetic force term also neglected, the momentum equation reduces to

$$0 = q_\sigma n_\sigma \mathbf{E} - \nabla P_\sigma - m_\sigma n_\sigma \nu_{\sigma n} \mathbf{u}, \quad (6)$$

where $P_\sigma \equiv n_\sigma k_B T_\sigma$. Eliminating $\mathbf{E}$ from the electron and ion momentum equations, solving for the particle flux, and substituting into the ion continuity equation, we arrive at the ambipolar diffusion equation

$$\frac{\partial n_e}{\partial t} - \frac{1}{m_i \nu_{in}} \nabla^2 P_e = \nu_{iz} n_e - K_{rec.} n_e^3, \quad (7)$$

where the ionization frequency ν_{iz} depends on the excited state populations and will be discussed in detail in the following text.

The derivation of Eq. (7) assumed that ν_{in} was a constant equal to $n_g \sigma_{in} v_{Ti}$; this is only true when $v_{Ti} \gg |\mathbf{u}|$. On the other hand, when $|\mathbf{u}| \gtrsim v_{Ti}$, the collision frequency depends on the bulk flow velocity, so Eq. (6) is nonlinear in $\mathbf{u}$, making the diffusion problem more difficult to solve. In the regime in which $\nu_{in} = n_g \sigma_{in} v_{Ti}$, the flow velocity is approximately

$$|\mathbf{u}| \approx \frac{|\nabla P_e|}{n_e m_i \nu_{in}} \sim \frac{k_B T_e}{l_{char.} m_i n_g \sigma_{in} v_{Ti}} = \frac{1}{2}\frac{T_e}{T_i}\frac{\lambda_{in}}{l_{char.}} v_{Ti}, \quad (8)$$

which shows that the assumption $|\mathbf{u}| < v_{Ti}$ is only self-consistent if $\lambda_{in}/l_{char.} \lesssim 2T_i/T_e$. This condition is satisfied in the axial direction in our discharge for $p_{Ar} \gtrsim 30\,\text{mTorr}$, which is the regime of interest for modeling the experiments, so Eq. (7) may be used.

Because the model is primarily concerned with the axial variation in plasma parameters, we will convert Eq. (7) to 1D by replacing $\nabla^2 P_e$ by $\partial^2 P_e/\partial z^2$. We account for the radial loss rate of plasma to the walls by adding an extra sink term on the right-hand side of the equation. In a cylindrical system, the ratio of the density at the radial sheath edge (defined as the location where the mean ion velocity toward the wall is equal to the ion acoustic speed, $c_s \equiv \sqrt{k_B T_e/m_i}$) to the peak density at the center of the plasma is given approximately by the following heuristic formula (Ref. 21, Sec. 3.4):

$$h_R(z) \equiv \frac{n_{sR}(z)}{n_{e,central}(z)} \approx 0.8\left(4 + \frac{R}{\lambda_{in}} + \frac{T_i}{T_e}\left(\frac{R}{\lambda_{in}}\right)^2\right)^{-1/2}, \quad (9)$$

where $\lambda_{in} = (n_g \sigma_{in})^{-1}$ is the ion-neutral collision mean free path. The accuracy of an analogous formula for planar geometry was recently verified by particle-in-cell simulations.[22] Equation (9) was derived by solving a steady state diffusion problem, but similar formulas have been used successfully by other authors in time-dependent problems.[3]

The flux into the radial sheath is $\Gamma(z) = n_{sR} c_s = h_R n_{e,central} c_s = 2h_R \langle n_e \rangle c_s$, so the loss rate per unit volume is $\Gamma(z)(2\pi R dz)/(\pi R^2 dz) = 2\Gamma(z)/R = 4h_R c_s \langle n_e \rangle / R$. Defining the effective radial loss frequency $\nu_{loss}(z) \equiv 4h_R c_s/R$, the ambipolar diffusion equation becomes

$$\frac{\partial n_e}{\partial t} - \frac{1}{m_i \nu_{in}}\frac{\partial^2 P_e}{\partial z^2} = (\nu_{iz} - \nu_{loss}) n_e - 2K_{rec.} n_e^3. \quad (10)$$

Here and in the derivations that follow, n_e and P_e should be understood to represent quantities averaged over the plasma cross section, but we are omitting angle brackets to reduce clutter in the equations. The radial averaging introduces an extra factor of 2 in the three-body recombination term because for a parabolic radial density profile, $\langle n_e^3 \rangle = 2\langle n_e \rangle^3$.

The ionization frequency ν_{iz} contains contributions from each of the electron-impact ionization processes illustrated in Fig. 3. Writing these out explicitly, we arrive at the final form of the axial diffusion equation for the model

$$\frac{\partial n_e}{\partial t} - \frac{1}{m_i \nu_{in}} \frac{\partial^2 P_e}{\partial z^2} = (K_{gi} n_g + K_{mi} n_m + K_{ri} n_r + K_{pi} n_p - \nu_{loss}) n_e - 2K_{rec.} n_e^3. \quad (11)$$

The electron pressure $P_e = n_e k_B T_e$ evolves according to the electron energy equation

$$\frac{\partial}{\partial t}\left(\frac{3}{2} P_e\right) + \nabla \cdot \left(\frac{3}{2} P_e \mathbf{u}\right) + P_e \nabla \cdot \mathbf{u} = p_{RF} - \nabla \cdot \mathbf{q}_e + m_e n_e \nu_{en} u^2 - \left(\frac{\partial W}{\partial t}\right)_{Een}, \quad (12)$$

where p_{RF} is the RF power input per unit volume. We will approximate the microscopic heat flux $\mathbf{q}_e$ using the Braginskii closure for the two-fluid equations,[23] which is valid when $\lambda_{ee} \ll l_{char.}$. In cgs units, the heat flux[24] is given by

$$\mathbf{q}_e = -\kappa_\parallel \nabla (k_B T_e); \quad \kappa_\parallel = 3.2 \frac{n_e k_B T_e}{m_e} \tau_e; \quad \tau_e = 1.7 \times 10^{23} \frac{(k_B T_e)^{3/2}}{n_e \ln\Lambda}. \quad (13)$$

Combining these expressions and converting to S.I. units, with T_e in eV and the Coulomb logarithm assumed to be $\ln\Lambda \approx 10$, the expression for the heat flux is

$$\mathbf{q}_e \approx -C_q \nabla (T_{eV}^{7/2}); \quad C_q \equiv 900\,\mathrm{kg\,m\,s^{-3}\,eV^{-3.5}}. \quad (14)$$

Following the same line of reasoning used to derive Eq. (10), we will convert the energy equation to 1D by rewriting the radial energy transport terms in terms of an effective energy sink term. The rate of radial energy loss per unit volume is equal to the loss rate of charged particles ($n_e \nu_{loss}$) times the energy carried to the walls by each electron-ion pair. It can be shown (Ref. 1, p. 37) that for a Maxwellian velocity distribution, the mean kinetic energy carried to the wall by each electron is $2k_B T_e$. The mean kinetic energy of each ion lost is $(k_B T_e/2 + eV_s)$, where the sheath voltage drop is $V_s \approx 4.7 k_B T_e/e$ for an inductively coupled argon discharge (Ref. 1, Sec. 10.2). The ion term must be included in the electron energy equation because the energy that accelerates the ions toward the wall is extracted from the difference between the plasma potential and the wall potential, which arises as a result of finite T_e. The 1D version of Eq. (12) is then

$$\frac{3}{2}\frac{\partial P_e}{\partial t} + \frac{3}{2}\frac{\partial}{\partial z}(P_e u_z) + P_e \frac{\partial u_z}{\partial z} = p_{RF} - \frac{\partial q_{ez}}{\partial z} + m_e n_e \nu_{en} u^2 - \left(\frac{\partial W}{\partial t}\right)_{Een} - n_e \nu_{loss}\left(eV_s + \frac{5}{2} k_B T_e\right). \quad (15)$$

Evaluating the magnitude of the frictional heating term using a typical radial diffusion velocity $u_r \sim v_{Ti} \approx 500\,\mathrm{m/s}$, we find

$$m_e n_e \nu_{en} u^2 \approx m_e n_e \nu_{en} u_r^2 \sim 1 \times 10^3\,\mathrm{W/m^3}, \quad (16)$$

where $n_e \sim 3 \times 10^{19}\,\mathrm{m^{-3}}$ was taken as a typical density value. On the other hand, the magnitude of the axial heat flux term is

$$-\frac{\partial q_{ez}}{\partial z} = C_q \frac{\partial^2}{\partial z^2}\left(T_{eV}^{7/2}\right) \sim \frac{C_q T_{eV}^{7/2}}{l_{char.}^2} \sim 4 \times 10^6\,\mathrm{W/m^3}, \quad (17)$$

so the frictional heating term is negligible by comparison. Using $u_{z,char.} \approx 120\,\mathrm{m/s}$ from Eq. (8), the ratio of the sum of the spatial derivative terms on the left-hand side of Eq. (15) to the time derivative term is

$$\frac{\frac{3}{2}\frac{\partial}{\partial z}(P_e u_z) + P_e \frac{\partial u_z}{\partial z}}{\frac{3}{2}\frac{\partial P_e}{\partial t}} \sim \frac{5}{3}\frac{u_{z,char.}}{\omega_{char.} l_{char.}} \sim 10^{-2}, \quad (18)$$

so the spatial derivative terms can be neglected. Thus Eq. (15) is simplified to

$$\frac{3}{2}\frac{\partial P_e}{\partial t} = p_{RF} + C_q \frac{\partial^2}{\partial z^2}\left(T_{eV}^{7/2}\right) - \left(\frac{\partial W}{\partial t}\right)_{Een} - n_e \nu_{loss}\left(eV_s + \frac{5}{2} k_B T_e\right). \quad (19)$$

$(\partial W/\partial t)_{Een}$, the collisional energy transfer from electrons to neutrals, includes collisional ionization, recombination, excitation/de-excitation, and elastic collisions. With these terms written out, the energy equation takes the form

$$\frac{3}{2}\frac{\partial P_e}{\partial t} = p_{RF} + \frac{C_q}{k_B^{7/2}} \frac{\partial^2}{\partial z^2}\left(\frac{P_e^{7/2}}{n_e^{7/2}}\right) - n_e \nu_{loss} e V_s - \frac{5}{2}\nu_{loss} P_e + 2K_{rec.} n_e^3 E_{pi} - n_e \left(K_{gi} n_g E_{gi} + K_{mi} n_m E_{mi} + K_{ri} n_r E_{ri} + K_{pi} n_p E_{pi} + \sum_{\alpha,\beta} K_{\alpha\beta} n_\alpha E_{\alpha\beta} + K_{el.} n_g E_{el.}\right). \quad (20)$$

The summation over α and β includes electron-impact de-excitations, which return energy to the free electrons, and excitations. The mean energy transfer per elastic electron-neutral collisions is $E_{el.} = (3m_e/M_i) k_B T_e$ (Ref. 1, p. 81). In the heat flux term, $k_B = 1.6 \times 10^{-19}\,\mathrm{J/eV}$ should be used if C_q is evaluated in the units given in Eq. (14).

We also need to track the evolution of the Ar I excited state population densities, which are determined by the excitation and de-excitation processes illustrated in Fig. 3. Axial diffusion of excited neutrals is neglected; however, we will include a term in each equation to account for radial losses of these atoms to the walls. The rate for this process is much lower than the collisional de-excitation rate in the region of interest near the center of the simulation domain (see Fig. 2),

but it can be important for preventing an unphysically high metastable population density from building up far from the antenna, where n_e is low and thus the metastable state is rarely depopulated by electron impacts. The loss rate[3,25] can be approximated by

$$\nu_{loss,exc.} \approx \frac{D_{eff.}}{\Lambda^2}, \tag{21}$$

where the effective diffusion length is $\Lambda = R/\chi_{01} = R/2.405$ (χ_{01} is the first zero of the Bessel function $J_0(x)$) and we will adopt Lee and Chung's[25] formula for the effective diffusion coefficient

$$D_{eff.} = \frac{1.0 \times 10^{20}\,\mathrm{m^2/s}}{n_g}. \tag{22}$$

The population equation for the $4s$ metastable state is

$$\frac{\partial n_m}{\partial t} = K_{gm} n_g n_e + K_{rm} n_r n_e + (K_{pm} n_e + A_{pm,eff.}) n_p - \left[(K_{mr} + K_{mp} + K_{mg} + K_{mi}) n_e + \frac{D_{eff.}}{\Lambda^2} \right] n_m, \tag{23}$$

the equation for the $4s$ resonant state is

$$\frac{\partial n_r}{\partial t} = K_{gr} n_g n_e + K_{mr} n_m n_e + (K_{pr} n_e + A_{pr,eff.}) n_p - \left[(K_{rm} + K_{rp} + K_{rg} + K_{ri}) n_e + A_{rg,eff.} + \frac{D_{eff.}}{\Lambda^2} \right] n_r, \tag{24}$$

and the equation for the $4p$ state is

$$\frac{\partial n_p}{\partial t} = K_{gp} n_g n_e + K_{mp} n_m n_e + K_{rp} n_r n_e + 2K_{rec.} n_e^3 - \left[(K_{pm} + K_{pr} + K_{pg} + K_{pi}) n_e + A_{pm,eff.} + A_{pr,eff.} + \frac{D_{eff.}}{\Lambda^2} \right] n_p. \tag{25}$$

In preparation for a numerical solution, we will rewrite Eqs. (11), (20), and (23)–(25) in dimensionless form by defining $\tau \equiv \nu_{in} t$, $\bar{z} \equiv z/z_0$, $\bar{n}_\alpha \equiv n_\alpha/n_0$, and $\bar{P}_e \equiv P_e/P_{e0} = n_e T_e/n_0 T_{e0}$. The radially averaged electron pressure $P_e = n_e k_B T_e$ is chosen as a primary simulation variable rather than T_e because it makes the calculation simpler overall, but $T_e(z,t)$ is also calculated at each time step so that the various temperature-dependent quantities (rate coefficients, etc.) in the equations can be evaluated. We also define the following dimensionless parameters:

$$A \equiv \frac{k_B T_{e0}}{m_i \nu_{in}^2 z_0^2}; \quad B(T_e) \equiv \frac{\nu_{loss}(T_e)}{\nu_{in}}; \quad C \equiv \frac{2}{3} \frac{C_q T_{e0}^{5/2}}{\nu_{in} n_0 k_B z_0^2}, \tag{26}$$

$$D(T_e) \equiv \frac{2}{3} \frac{\nu_{loss}(T_e) e V_s(T_e)}{\nu_{in} k_B T_{e0}}; \quad E(T_e) \equiv \frac{5}{3} \frac{\nu_{loss}(T_e)}{\nu_{in}}, \tag{27}$$

$$\bar{K}_{\alpha\beta}(T_e) \equiv \frac{K_{\alpha\beta}(T_e) n_0}{\nu_{in}}; \quad \bar{K}_{E\alpha\beta}(T_e) \equiv \frac{2}{3} \frac{K_{\alpha\beta}(T_e) n_0 E_{\alpha\beta}}{\nu_{in} k_B T_{e0}}, \tag{28}$$

$$\bar{K}_{rec.} \equiv \frac{2K_{rec.}(T_e) n_0^2}{\nu_{in}}; \quad \bar{K}_{E,rec.} \equiv \frac{4}{3} \frac{K_{rec.}(T_e) n_0^2 E_{pi}}{\nu_{in} k_B T_{e0}}, \tag{29}$$

$$\bar{p}_{RF} \equiv \frac{2}{3} \frac{p_{RF}}{\nu_{in} n_0 k_B T_{e0}}; \quad \bar{D}_{eff.} \equiv \frac{D_{eff.}}{\Lambda^2 \nu_{in}}; \quad \bar{A}_{\alpha\beta} \equiv \frac{A_{\alpha\beta,eff.}}{\nu_{in}}. \tag{30}$$

Here, T_{e0} is in eV and k_B is in J/eV, but $E_{\alpha\beta}$ is in J. With these definitions, the five equations that must be solved for the unknowns $\bar{n}_e$, $\bar{P}_e$, $\bar{n}_m$, $\bar{n}_r$, and $\bar{n}_p$ are

$$\frac{\partial \bar{n}_e}{\partial \tau} = A \frac{\partial^2 \bar{P}_e}{\partial \bar{z}^2} - B \bar{n}_e + \left(\bar{K}_{gi} \bar{n}_g + \bar{K}_{mi} \bar{n}_m + \bar{K}_{ri} \bar{n}_r + \bar{K}_{pi} \bar{n}_p \right) \bar{n}_e - \bar{K}_{rec.} \bar{n}_e^3, \tag{31}$$

$$\frac{\partial \bar{P}_e}{\partial \tau} = \bar{p}_{RF} + C \frac{\partial^2}{\partial \bar{z}^2} \left(\frac{\bar{P}_e^{7/2}}{\bar{n}_e^{7/2}} \right) - D \bar{n}_e - E \bar{P}_e + \bar{K}_{E,rec.} \bar{n}_e^3 - \bar{n}_e \left(\bar{K}_{Egi} \bar{n}_g + \bar{K}_{Emi} \bar{n}_m + \bar{K}_{Eri} \bar{n}_r + \bar{K}_{Epi} \bar{n}_p + \sum_{\alpha,\beta} \bar{K}_{E\alpha\beta} \bar{n}_\alpha + \bar{K}_{Eel.} \bar{n}_g \right), \tag{32}$$

$$\frac{\partial \bar{n}_m}{\partial \tau} = \bar{K}_{gm} \bar{n}_g \bar{n}_e + \bar{K}_{rm} \bar{n}_r \bar{n}_e + \left(\bar{K}_{pm} \bar{n}_e + \bar{A}_{pm} \right) \bar{n}_p - \left[\left(\bar{K}_{mr} + \bar{K}_{mp} + \bar{K}_{mg} + \bar{K}_{mi} \right) \bar{n}_e + \bar{D}_{eff.} \right] \bar{n}_m, \tag{33}$$

$$\frac{\partial \bar{n}_r}{\partial \tau} = \bar{K}_{gr} \bar{n}_g \bar{n}_e + \bar{K}_{mr} \bar{n}_m \bar{n}_e + \left(\bar{K}_{pr} \bar{n}_e + \bar{A}_{pr} \right) \bar{n}_p - \left[\left(\bar{K}_{rm} + \bar{K}_{rp} + \bar{K}_{rg} + \bar{K}_{ri} \right) \bar{n}_e + \bar{A}_{rg} + \bar{D}_{eff.} \right] \bar{n}_r, \tag{34}$$

$$\frac{\partial \bar{n}_p}{\partial \tau} = \bar{K}_{gp} \bar{n}_g \bar{n}_e + \bar{K}_{mp} \bar{n}_m \bar{n}_e + \bar{K}_{rp} \bar{n}_r \bar{n}_e + \bar{K}_{rec,} \bar{n}_e^3 - \left[\left(\bar{K}_{pm} + \bar{K}_{pr} + \bar{K}_{pg} + \bar{K}_{pi} \right) \bar{n}_e + \bar{A}_{pm} + \bar{A}_{pr} + \bar{D}_{eff.} \right] \bar{n}_p. \tag{35}$$

The numerical algorithm used to advance these equations forward in time is described in the Appendix. After solving for the electron density and the excited state populations at each time step, the ground state neutral density is calculated from $\bar{n}_g = n_{total}/n_0 - (\bar{n}_e + \bar{n}_m + \bar{n}_r + \bar{n}_p)$.

IV. RESULTS

A. Ion saturation current

To validate the model, the numerical results were compared with ion saturation currents ($I_{sat.}$) measured by the Langmuir probe. The simulated $I_{sat.}(t)$ was calculated from $n_i(t)$ and $T_e(t)$ using the formula:

$$I_{sat.} = \frac{n_i e A i_{+-} c_s}{\sqrt{2\pi}}, \tag{36}$$

where A is the probe surface area in the experiment and i_{+-} is a dimensionless correction factor obtained from numerical ion orbit calculations by Laframboise.[26] i_{+-} is a function of $e(V_{probe} - V_{plasma})/k_B T_e$ and r_{probe}/λ_{De}, where $\lambda_{De} \equiv \sqrt{\epsilon_0 k_B T_e / n_e e^2}$ is the electron Debye length. Values of V_{probe}

and r_{probe} from the corresponding experiments were used to calculate $I_{sat.}$ in the simulations. The value of $i_{+-}/\sqrt{2\pi}$ ranged from 0.4 to 1.1 over the parameter range of interest, which may be compared with the commonly used approximation $I_{sat.} \approx 0.6 n_i e A c_s$.[27] The probe measurements were made on axis, so Eq. (36) was evaluated using $n_{i,central}$, which was twice the radially averaged density n_i calculated in the simulation. The peak RF power level in the simulation and the rate of decay of the absorbed power (P_{RF} decreased in time in the experiment due to the gradual discharging of the battery-powered RF amplifier's final stage capacitor) were adjusted so that the model $I_{sat.}(t)$ matched the data at $z = -7$ cm, the furthest location inside the antenna at which data was taken. The accuracy of the model was then judged by the extent to which the predicted $I_{sat.}(t)$ downstream at $z = -6$ cm to $z = -0$ cm matched the measurements.

$T_i = T_g$ was adjusted within the plausible range 0.025–0.25 eV for the best fit to the data. Changing T_i affected the ambipolar diffusion rate through the dependence of the ion-neutral collision frequency ν_{in} on v_{Ti} (see Eq. (11)), while T_g influenced the cross sections for re-absorption of line emission (see Eq. (3)). An example of the impact of varying the ion/neutral temperature on $I_{sat.}$ is shown in Fig. 4.

The best-fit model results for $p_{Ar} = 30$ mTorr and 60 mTorr are shown overlaid on the Langmuir probe data in Figs. 5 and 6. There are four main properties of the experimental $I_{sat.}$ curves that a model should ideally reproduce: the time delay before the density begins to rise at each axial location, the rate of increase $\partial I_{sat.}/\partial t$ during the density rise, the final quasi-steady state axial $I_{sat.}(z)$ profile, and the rate of decrease of $I_{sat.}$ after RF power turn-off. As seen in Figs. 5 and 6, our model performed excellently by the second and third measures and reasonably well by the fourth. The quasi-steady state $I_{sat.}(z)$ profile matched the data closely, and the rate at which $I_{sat.}$ rose at each location was predicted nearly perfectly as well.

However, in the simulations, the plasma density both within the antenna and downstream began to rise soon after the RF power was turned on, while in reality there was a delay of $\sim 5 - 10\,\mu$s before $I_{sat.}$ began to rise at each successive axial location. Only if the model $I_{sat.}(t)$ curves are artificially translated in time, as in Figs. 5(b) and 6(b), is the excellent agreement in $\partial I_{sat.}/\partial t$ at each location demonstrated. The reason for the immediate downstream density rise in the model can be seen from the detailed results presented in Sec. IV B. At the beginning of the discharge, the plasma density is low, and the high level of RF power input causes T_e to become high inside the antenna. The resulting gradient in T_e leads to a large axial heat flux (see Eqs. (14) and (20)) that quickly raises the temperature downstream

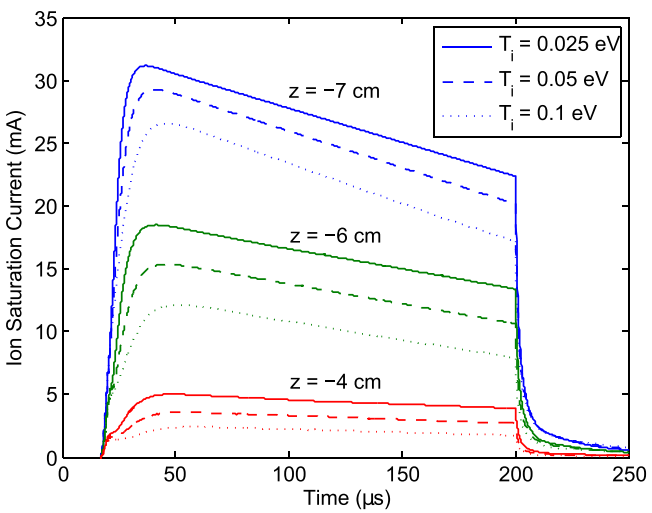

FIG. 4. $I_{sat.}(z,t)$ at $r = 0$ cm calculated by the model for three different ion/neutral temperatures. The gas pressure was $p_{Ar} = 30$ mTorr and the peak absorbed power was $P_{RF} = 1620$ W.

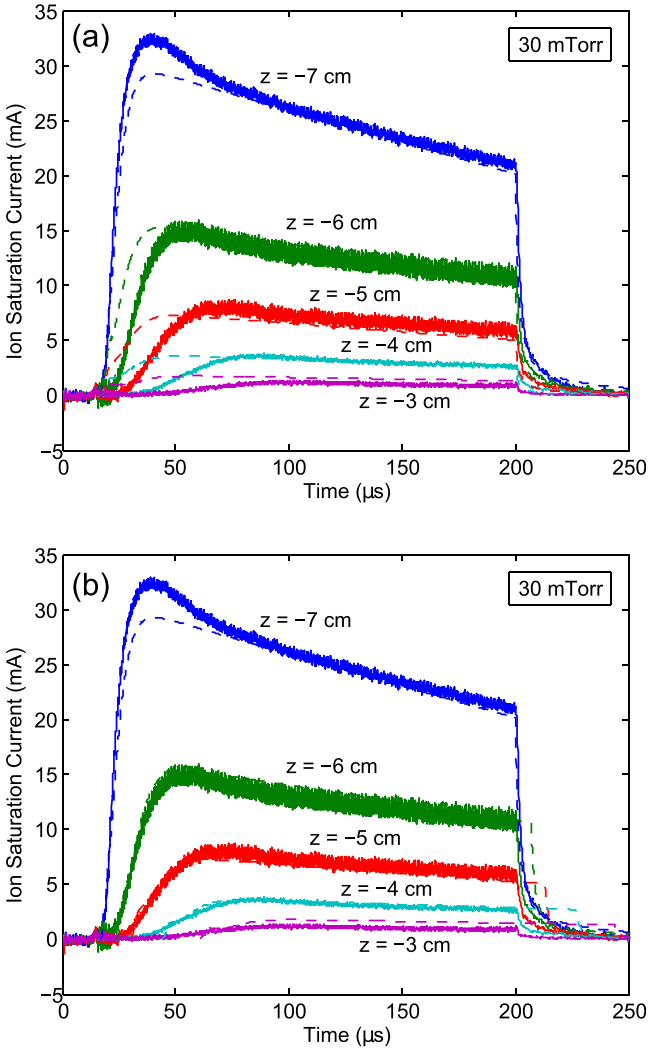

FIG. 5. Model $I_{sat.}$ predictions (dashed curves) overlaid on Langmuir probe data (solid curves) for discharges at $p_{Ar} = 30$ mTorr. The time dependence of the RF power input after the initial 3 μs ramp-up period was modeled as $P_{RF}(t) = (1620\,\text{W})[1 - (t - t_{peak})/(750\,\mu\text{s})]$, and the best fit between the model and data was achieved with $T_i = 0.05$ eV. The timing of power turn-on ($t = 17\,\mu$s) was set to coincide with the initial fast density rise at $z = -7$ cm in the experiment, and the power was turned off at $t = 200\,\mu$s. In panel (a), the raw model results are shown, while in panel (b), the downstream model curves ($z = -6$ cm to $z = -3$ cm) have been shifted in time to match the measured timing of the initial density rise at each location in order to demonstrate the excellent agreement in the calculated and measured $\partial I_{sat.}/\partial t$ (the model curves at $z = -6$ cm through $z = -4$ cm are not visible because they overlap the data nearly exactly).

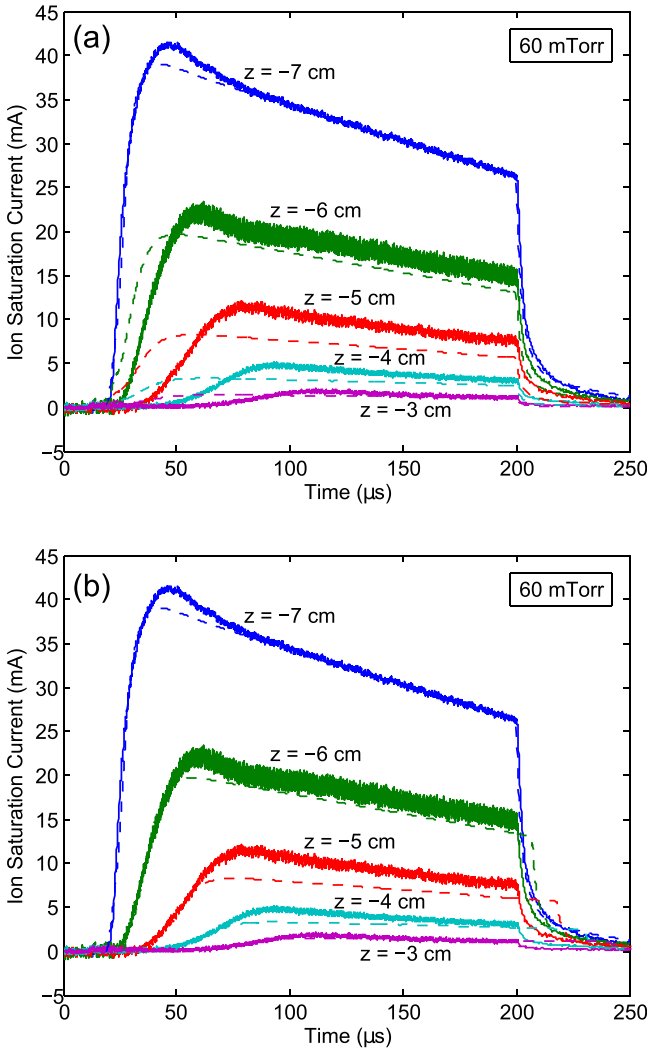

FIG. 6. Same as Fig. 5, but for $p_{Ar} = 60\,\text{mTorr}$. The best fit between the model and data was achieved with $T_i = 0.03\,\text{eV}$ and $P_{RF,peak} = 1290\,\text{W}$.

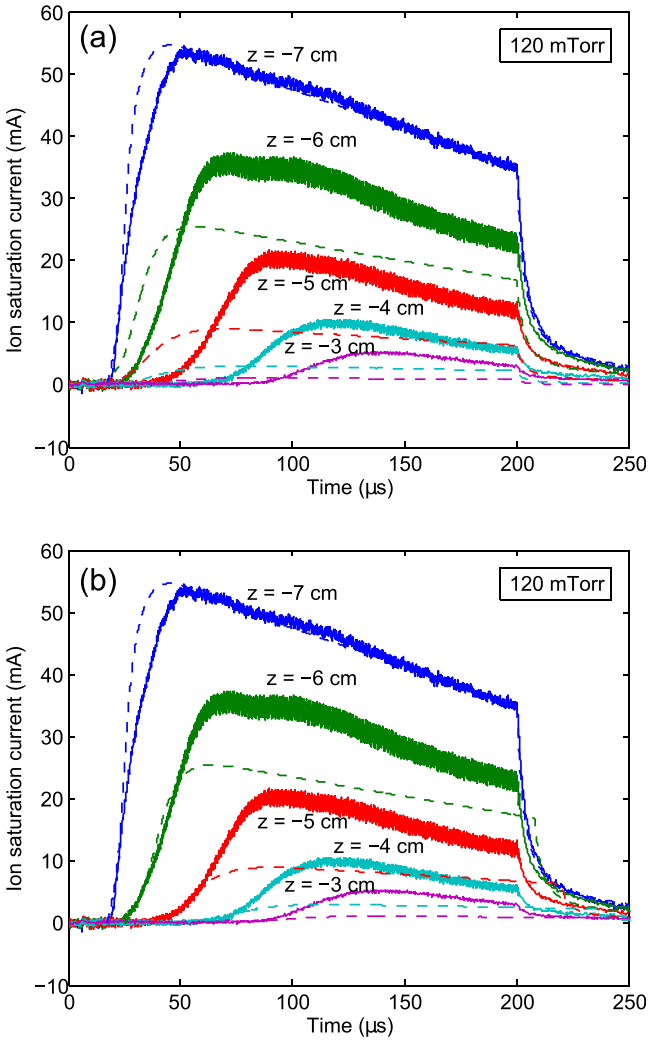

FIG. 7. Same as Fig. 5, but for $p_{Ar} = 120\,\text{mTorr}$. The best fit between the model and data was achieved with $T_i = 0.025\,\text{eV}$ and $P_{RF,peak} = 1060\,\text{W}$.

(see Fig. 8). With $T_e \sim 5\,\text{eV}$ and $n_g \approx 10^{21}\,\text{m}^{-3}$, the ionization rate is $K_{gi}n_g \sim 2 \times 10^6\,\text{s}^{-1}$. This is much larger that the radial loss rate $\nu_{loss} = 4h_R c_s/R \sim 3 \times 10^5\,\text{s}^{-1}$, so Eq. (11) approximately reduces to $\partial n_e \partial t \approx K_{gi}n_g n_e$, implying that n_e grows exponentially with a time constant of $\sim$500 ns until the electrons have cooled enough to reduce the ionization rate (this argument neglects stepwise ionization, so the actual e-folding time would be even shorter).

This sequence of events probably did not occur in the experiments because the electron heat flux q_{ez} could not actually be high in regions where there was little or no plasma present. The Braginskii heat flux expression (Eq. (14)) is independent of n_e, but it was derived under the assumption of a collisional plasma ($\lambda_{ee} \ll l_{char.}$) and thus is not valid in the region out in front of the expanding plasma. However, it is not clear what expression for the heat flux should be used instead of Eq. (14) in this region; more work is needed to determine whether this aspect of the plasma transport can be accurately modeled within a two-fluid framework.

The model results for $p_{Ar} = 120\,\text{mTorr}$ are compared with probe data in Fig. 7. Although the model matches the measured rise and fall rates of $I_{sat.}$ reasonably well, the predicted quasi-steady state $I_{sat.}(z)$ declines too quickly moving away from the power deposition region. This discrepancy between the model and data became more severe for simulations at even higher pressures. Therefore there must be some physical process missing from the model that is relatively unimportant at $p \lesssim 60\,\text{mTorr}$ but becomes critical for achieving a high downstream density at $p \gtrsim 120\,\text{mTorr}$. One possibility is stepwise ionization out of excited states higher than $4p$; we would expect that states with energies within $\sim k_B T_e$ of the ionization energy could be neglected without introducing much error in the calculated ionization rate, but this criterion becomes more difficult to satisfy at higher pressures because the equilibrium T_e falls. The best way to test this hypothesis would be to construct a more complex model with additional energy levels included.

B. Plasma parameters and excited state populations

The close agreement between the predicted $I_{sat.}$ and the probe data at $p_{Ar} = 30 - 60\,\text{mTorr}$ provides confidence that

the key physical processes in this pressure range are well understood. In this regime, the simulation results can offer insights into plasma properties and atomic processes that could not be measured with the available diagnostics. Some examples will be shown from the calculations at 60 mTorr—qualitatively similar results were obtained at 30 mTorr.

Figure 8 shows the time evolution of the electron temperature, which could not be measured accurately using the uncompensated single Langmuir probe. When the power is turned on, T_e rises rapidly to $\sim$9 eV everywhere and then gradually falls to an equilibrium value of 2.0–2.2 eV. Overshoot in T_e at the beginning of the pulsed discharge is a universal prediction of ICP models.[2] Axial heat flux keeps the plasma nearly isothermal, but the slight temperature gradient is important for establishing the quasi-steady state density profile observed in Fig. 6. After RF power turn-off at $t = 200\ \mu$s, T_e falls very quickly to $<$0.2 eV.

The calculated excited state population densities for the same discharge conditions are shown in Fig. 9. The high electron temperature at early times leads to a high rate of collisional excitation that quickly raises n_m, n_r, and n_p, enabling a high stepwise ionization rate that builds up the plasma density. The excited state populations fall moving away from the power deposition region. The 4*s* metastable and 4*s* resonant manifolds have similar population densities because the collisional transition rate between these states is high and most of the resonant line emission is re-absorbed. In the quasi-steady state, the 4*p* level has a higher population

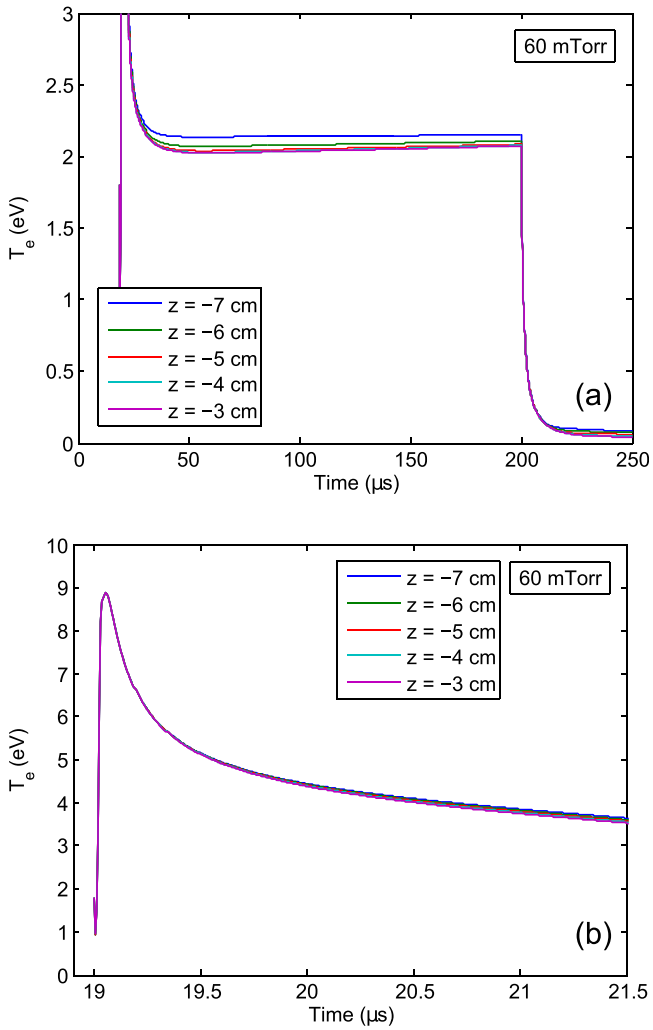

FIG. 8. Calculated electron temperature vs. time at $p_{Ar} = 60$ mTorr. The same simulation parameters were used as in Fig. 6. Panel (b) zooms in on the first 2.5 μs of the simulation, which was started at $t = 19\ \mu$s to facilitate comparison with the data in Fig. 6.

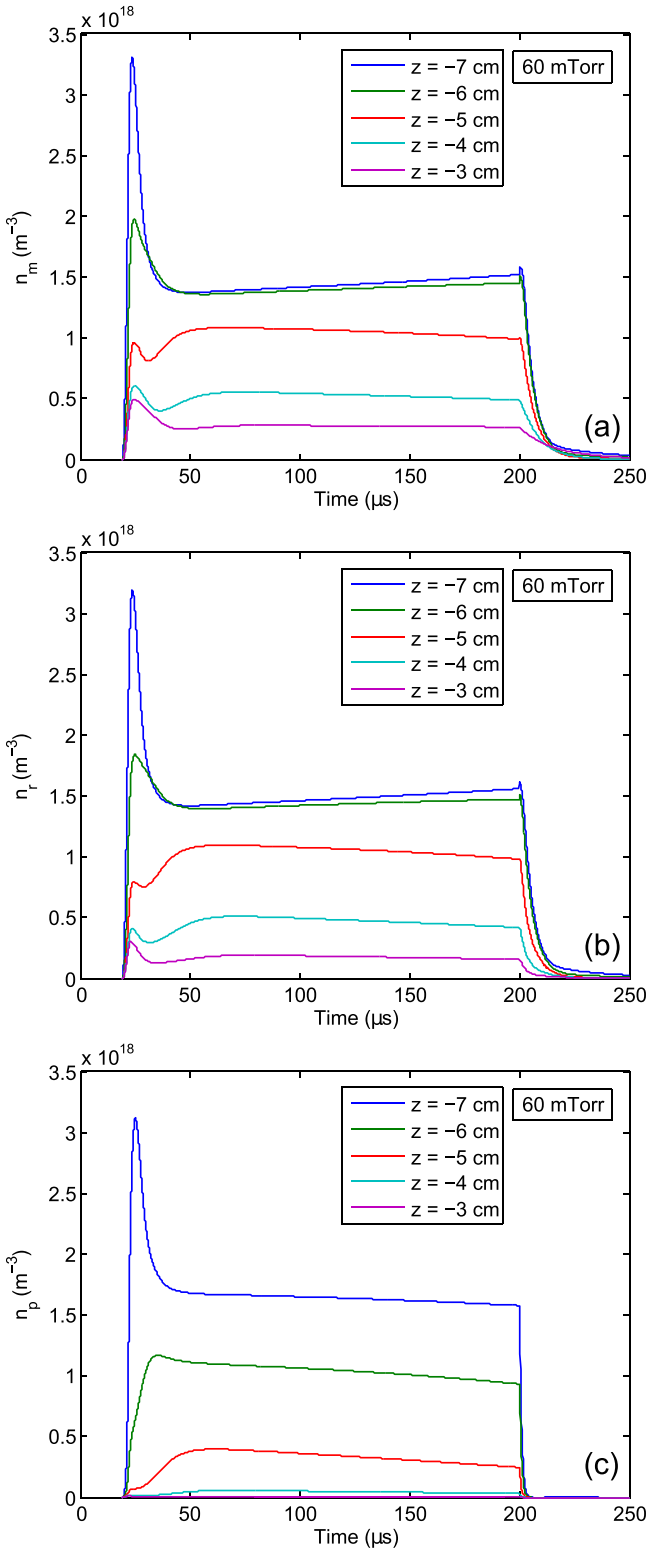

FIG. 9. Calculated Ar I excited state population densities vs. time at $p_{Ar} = 60$ mTorr. The same simulation parameters were used as in Fig. 6.

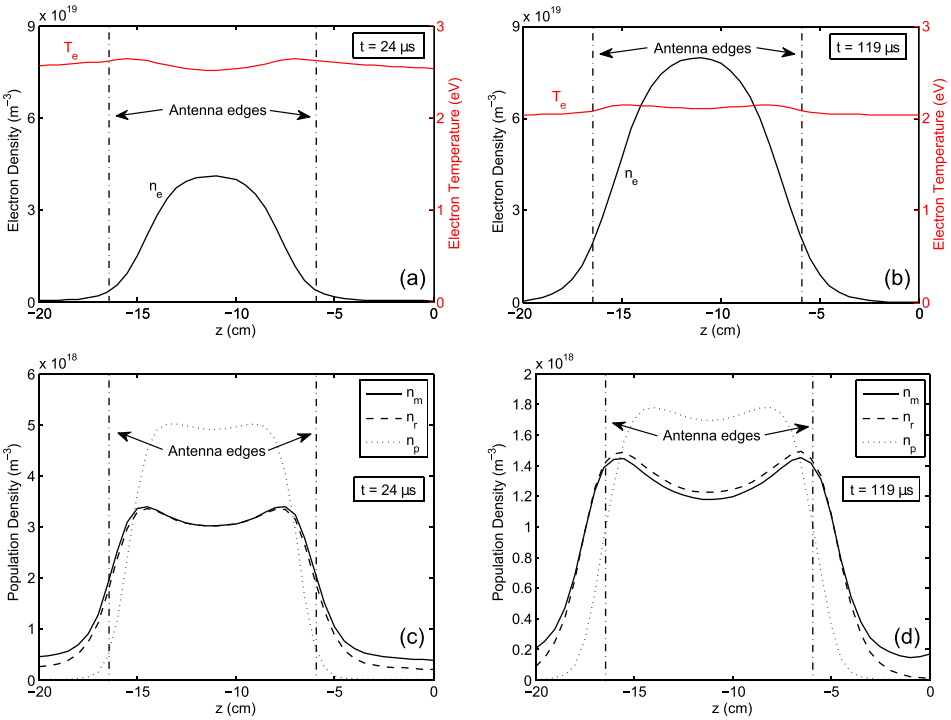

FIG. 10. Spatial dependence of n_e, T_e, n_m, n_r, and n_p at $p_{Ar} = 60$ mTorr. The same simulation parameters were used as in Fig. 6. The profiles are plotted at $t = 24\,\mu$s (i.e., 5 μs after the start of the simulation) and at $t = 119\,\mu$s, during the quasi-steady state phase.

density than the $4s$ levels well inside the antenna, but n_p decreases more rapidly moving downstream.

The spatial profiles of the plasma density, electron temperature, and excited state population densities are plotted for two representative times in Fig. 10. After the initial transient phase of the discharge, T_e is approximately uniform inside the power deposition region and approximately uniform far downstream, but there is a relatively steep temperature gradient in the transition regions around $z \sim -15.9$ cm and $z \sim -6.4$ cm that drives heat flux away from the antenna. Interestingly, n_m, n_r, and n_p peak near the edges of the power deposition region and are lower at the center of the antenna due to the complex balance of populating and de-populating processes included in Eqs. (23)–(25). It is also notable that there is a substantial population density of metastable excited atoms far from the antenna region.

C. Energy budget

A useful feature of numerical modeling is the ability to plot the magnitude of each term in the equations as a function of time or position to monitor their relative importance. One example is given in Fig. 11, which illustrates the contributions of the various terms in Eq. (32) to the overall rate of change of the dimensionless electron pressure at $z = -5$ cm. Figure 11(a) shows that heat flux from the antenna region is approximately balanced by the sum of diffusive energy losses to the walls (the terms involving D and E in Eq. (32)) and electron energy losses due to inelastic collisions (the ionization and excitation/de-excitation terms in Eq. (32)) during the main discharge. In the afterglow (Fig. 11(b)), diffusive losses to the walls (i.e., evaporative cooling) are the dominant energy loss mechanism, and three-body recombination provides some reheating of the electrons. The effect of elastic electron-neutral collisions is negligible during both periods.

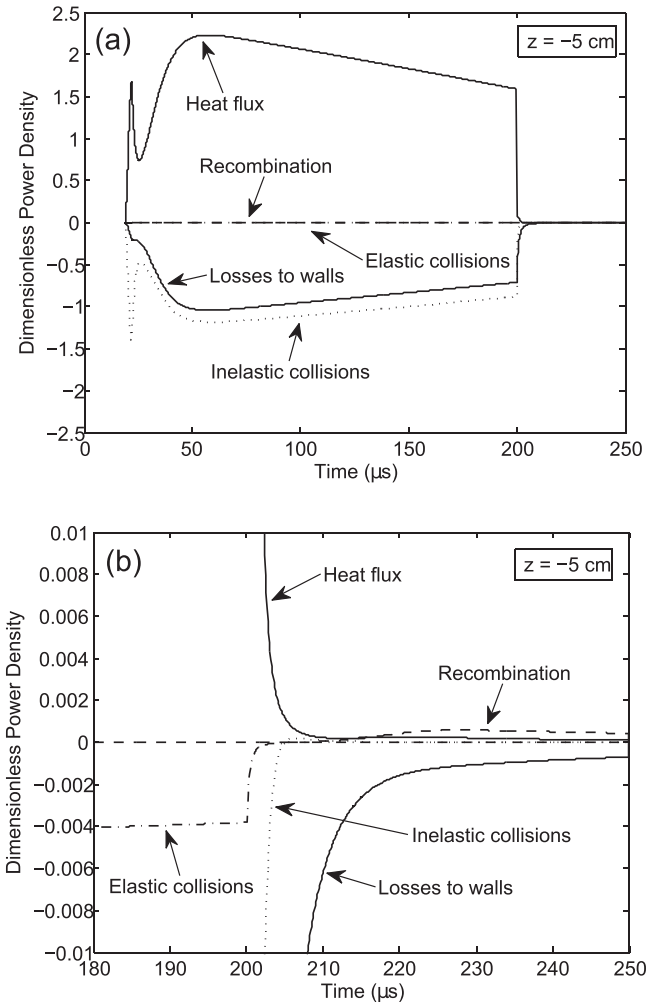

FIG. 11. Relative contributions of the processes included in Eq. (32) to the overall $\partial \bar{P}_e/\partial \tau$ at $z = -5$ cm, just downstream of the power deposition region. Panel (b) zooms in on the afterglow period ($t > 200\,\mu$s). The same simulation parameters were used as in Fig. 6.

V. CONCLUSION

We have described a time-dependent numerical fluid model of a high-density inductively coupled plasma in a long, narrow discharge tube. The ambipolar diffusion equation, electron energy equation, and excited state population equations were solved in the axial direction, and radial particle and energy losses were accounted for by using a well-known formula for the ratio of the sheath edge density to the central density to calculate an effective radial loss frequency. The simulation was validated through comparisons with Langmuir probe ion saturation current measurements, and excellent agreement in the plasma density rise time and quasi-steady state spatial density profile was obtained at 30–60 mTorr. At higher pressures, the model underestimated the density downstream of the antenna. The simulation results contained detailed information about the plasma parameters, excited state populations, energy budget, and other quantities, presenting a clear picture of the most important physical processes during each stage of the discharge. However, the details of the physics at the expansion front are not yet understood.

The approach we have used for converting a 2D or 3D problem to 1D while incorporating the effect of losses in the remaining directions should be applicable to modeling other experiments in which variations in the plasma parameters in a particular direction are of predominant interest. The simulations run in a few minutes on a typical desktop PC, enabling a large number of calculations with varying parameters to be carried out quickly for efficient experiment design or parameter tuning. In plasma processing, the substrate is usually located downstream of the coil or antenna, so a model similar to ours could reveal useful information that cannot be obtained from global discharge models.

ACKNOWLEDGMENTS

This material is based upon work supported by the U.S. Department of Energy Office of Science, Office of Fusion Energy Sciences under Award Nos. DE-FG02-04ER54755 and DE-SC0010471 and by the National Science Foundation under Award No. 1059519. V. H. Chaplin acknowledges support by the ORISE Fusion Energy Sciences Graduate Fellowship.

APPENDIX: NUMERICAL ALGORITHM

Equations (31)–(35) were discretized with a spatial grid spacing h_z and time step h_t using a standard second-order finite difference formula for the spatial derivatives and a first-order difference formula for the time derivatives. Labeling the spatial grid point and the time step by superscripts i and j, respectively, the discretized form of Eq. (31) is

$$\bar{n}_e^{i,j} = \frac{h_t A}{h_z^2}\left(\bar{P}_e^{i+1,j} - 2\bar{P}_e^{i,j} + \bar{P}_e^{i-1,j}\right) + W^{i,j-1}, \tag{A1}$$

$$W^{i,j-1} \equiv \bar{n}_e^{i,j-1}\left[1 + h_t\left(\sum_\alpha \bar{K}_{\alpha i}^{i,j-1}\bar{n}_\alpha^{i,j-1} - B^{i,j-1} - \bar{K}_{rec.}^{i,j-1}(\bar{n}_e^{i,j-1})^2\right)\right]. \tag{A2}$$

The terms arising from the second-order spatial derivative are treated implicitly (i.e., they are evaluated at time j instead of at time $j-1$) to avoid the oscillatory numerical instabilities that develop when diffusion-like equations are advanced in time using explicit methods.[28] The remaining terms, which we group together as $W^{i,j-1}$, may safely be evaluated explicitly.

Similarly, Eq. (32) is discretized as

$$P_e^{i,j} = \frac{h_t C}{h_z^2}\left[\left(\frac{\bar{P}_e^{i+1,j}}{\bar{n}_e^{i+1,j}}\right)^{7/2} - 2\left(\frac{\bar{P}_e^{i,j}}{\bar{n}_e^{i,j}}\right)^{7/2} + \left(\frac{\bar{P}_e^{i-1,j}}{\bar{n}_e^{i-1,j}}\right)^{7/2}\right] + V^{i,j-1}, \tag{A3}$$

where

$$V^{i,j-1} \equiv h_t \bar{p}_{RF}^{i,j-1} + \bar{P}_e^{i,j-1}(1 - h_t E^{i,j-1}) + h_t \bar{n}_e^{i,j-1} \times \left(\bar{K}_{E,rec.}^{i,j-1}(\bar{n}_e^{i,j-1})^2 - D^{i,j-1} - \sum_\alpha \bar{K}_{E\alpha i}^{i,j-1}\bar{n}_\alpha^{i,j-1} - \sum_{\alpha\beta}\bar{K}_{E\alpha\beta}^{i,j-1}\bar{n}_\alpha^{i,j-1} - \bar{K}_{Eel.}^{i,j-1}\bar{n}_g^{i,j-1}\right). \tag{A4}$$

The unknown electron densities at time j may be eliminated from the system of equations by substituting Eq. (A1) into Eq. (A3)

$$P_e^{i,j} = \frac{h_t C}{h_z^2}\left[\left(\frac{\bar{P}_e^{i+1,j}}{\frac{h_t A}{h_z^2}\left(\bar{P}_e^{i+2,j} - 2\bar{P}_e^{i+1,j} + \bar{P}_e^{i,j}\right) + W^{i+1,j-1}}\right)^{7/2} - 2\left(\frac{\bar{P}_e^{i,j}}{\frac{h_t A}{h_z^2}\left(\bar{P}_e^{i+1,j} - 2\bar{P}_e^{i,j} + \bar{P}_e^{i-1,j}\right) + W^{i,j-1}}\right)^{7/2} + \left(\frac{\bar{P}_e^{i-1,j}}{\frac{h_t A}{h_z^2}\left(\bar{P}_e^{i,j} - 2\bar{P}_e^{i-1,j} + \bar{P}_e^{i-2,j}\right) + W^{i-1,j-1}}\right)^{7/2}\right] + V^{i,j-1}. \tag{A5}$$

This equation is valid for $2 \le i \le N_z - 3$. At the points adjacent to the boundaries ($i = 1$ and $i = N_z - 2$), either $\bar{P}_e^{i-2,j}$ or $\bar{P}_e^{i+2,j}$ is outside the simulation domain, and the boundary value $\bar{n}_e^{0,j}$ or $\bar{n}_e^{N_z-1,j}$ should be used in the denominator of the appropriate term in Eq. (A5) instead of substituting in from Eq. (A1). The pressures at the boundaries are determined by the zero heat flux boundary condition $\partial T_e/\partial \bar{z} = 0$. Taylor expansions of $T_e^{1,j}$ and $T_e^{2,j}$ about the boundary location $\bar{z}^0$ can be combined to derive the following discretized form of this condition:

$$T_e^{0,j} = \frac{4T_e^{1,j} - T_e^{2,j}}{3}. \tag{A6}$$

The dimensionless pressure at $\bar{z}^0$ can then be evaluated as

$$\bar{P}_e^{0,j} = \frac{\bar{n}_e^{0,j}T_e^{0,j}}{T_{e0}} = \frac{\bar{n}_e^{0,j}}{T_{e0}}\left(\frac{4T_e^{1,j} - T_e^{2,j}}{3}\right) = \frac{\bar{n}_e^{0,j}}{3}\left(\frac{4\bar{P}_e^{1,j}}{\bar{n}_e^{1,j}} - \frac{\bar{P}_e^{2,j}}{\bar{n}_e^{2,j}}\right), \tag{A7}$$

$$= \frac{\bar{n}_e^{0,j}}{3}\left(\frac{4\bar{P}_e^{1,j}}{\frac{h_t A}{h_z^2}\left(\bar{P}_e^{2,j} - 2\bar{P}_e^{1,j} + \bar{P}_e^{0,j}\right) + W^{1,j-1}} - \frac{\bar{P}_e^{2,j}}{\frac{h_t A}{h_z^2}\left(\bar{P}_e^{3,j} - 2\bar{P}_e^{2,j} + \bar{P}_e^{1,j}\right) + W^{2,j-1}}\right). \quad \text{(A8)}$$

The corresponding formula at $\bar{z}^{N_z-1}$ is

$$\bar{P}_e^{N_z-1,j} = \frac{\bar{n}_e^{N_z-1,j}}{3}\left(\frac{4\bar{P}_e^{N_z-2,j}}{\frac{h_t A}{h_z^2}\left(\bar{P}_e^{N_z-1,j} - 2\bar{P}_e^{N_z-2,j} + \bar{P}_e^{N_z-3,j}\right) + W^{N_z-2,j-1}} - \frac{\bar{P}_e^{N_z-3,j}}{\frac{h_t A}{h_z^2}\left(\bar{P}_e^{N_z-2,j} - 2\bar{P}_e^{N_z-3,j} + \bar{P}_e^{N_z-4,j}\right) + W^{N_z-3,j-1}}\right). \quad \text{(A9)}$$

Equations (A5), (A8), and (A9) make up a system of N_z nonlinear algebraic equations, which were solved at each time step using Newton's method. The solution for $\bar{P}_e^{i,j}$ was then used in Eq. (A1) to determine $\bar{n}_e^{i,j}$.

Because Eqs. (33)–(35) for the excited state population densities contain no spatial derivatives, they could be advanced in time explicitly. However, to maintain stability, it was necessary for the time step to be small enough that h_t multiplied by each rate term in the equations was much smaller than the population density $\bar{n}_\alpha^{i,j-1}$ at the previous time step. Because of the high collisional transition rates between the excited states, this criterion was more difficult to satisfy than the requirement on h_t for overall accuracy of the calculation, so each time step was broken up into sub-time steps of size $h_t/10$ for the purpose of evolving Eqs. (33)–(35), while $\bar{P}_e$ and $\bar{n}_e$ were only updated at intervals separated by h_t. A small value of h_t (typically 5–10 ns in physical units) was required early in the simulation when $\bar{P}_e(\bar{z},\tau)$ and other variables were changing quickly, while setting $h_t = 100$ ns was sufficient after the discharge had reached a nearly steady state.

[1]M. A. Lieberman and A. J. Lichtenberg, *Principles of Plasma Discharges and Materials Processing*, 2nd edn. (Wiley-Interscience, Hoboken, NJ, 2005).
[2]S. Banna, A. Agarwal, G. Cunge, M. Darnon, E. Pargon, and O. Joubert, J. Vac. Sci. Technol. B **30**(4), 040801 (2012).
[3]S. Ashida, C. Lee, and M. A. Lieberman, J. Vac. Sci. Technol. A **13**(5), 2498 (1995).
[4]M. H. Lee and C. W. Chung, Appl. Phys. Lett **87**, 131502 (2005).
[5]B. Ramamurthi and D. J. Economou, Plasma Sources Sci. Technol. **11**, 324 (2002).
[6]P. Subramonium and M. J. Kushner, J. Vac. Sci. Technol. A **20**(2), 313 (2002).
[7]P. Subramonium and M. J. Kushner, J. Appl. Phys. **96**(1), 82 (2004).
[8]R. S. Wise, D. P. Lymberopoulos, and D. J. Economou, Appl. Phys. Lett. **68**(18), 2499 (1996).
[9]S. C. Hsu and P. M. Bellan, Phys. Plasmas **12**, 032103 (2005).
[10]V. H. Chaplin and P. M. Bellan, Rev. Sci. Instrum. **86**, 073506 (2015).
[11]D. P. Lymberopoulos, V. I. Kolobov, and D. J. Economou, J. Vac. Sci. Technol. A **16**(2), 564 (1998).
[12]J. Henriques, E. Tatarova, F. M. Dias, and C. M. Ferreira, J. Appl. Phys. **90**(10), 4921 (2001).
[13]T. Shoji, Y. Sakawa, S. Nakazawa, K. Kadota, and T. Sato, Plasma Sources Sci. Technol. **2**, 5 (1993).
[14]Y. Celik, T. V. Tsankov, M. Aramaki, S. Yoshimura, D. Luggenhölscher, and U. Czarnetzki, Phys. Rev. E **85**, 056401 (2012).
[15]A. Kramida, Y. Ralchenko, J. Reader, and NIST ASD Team, See http://physics.nist.gov/asd for NIST Atomic Spectra Database (ver. 5.1), National Institute of Standards and Technology, Gaithersburg, MD, 2013.
[16]G. B. Rybicki and A. P. Lightman, *Radiative Processes in Astrophysics*, 2nd ed. (Wiley-VCH, Germany, 2004).
[17]V. H. Chaplin, "Battery-powered RF pre-ionization system for the Caltech magnetohydrodynamically-driven jet experiment: RF discharge properties and MHD-driven jet dynamics," Ph.D. thesis, California Institute of Technology, 2015.
[18]P. M. Bellan, *Fundamentals of Plasma Physics* (Cambridge University Press, New York, 2006).
[19]N. Sternberg and V. Godyak, Plasma Sources Sci. Technol. **20**, 015018 (2011).
[20]J. H. Palacio Mizrahi, V. Tz. Gurovich, and Ya. E. Krasik, Phys. Plasmas **20**, 032116 (2013).
[21]P. Chabert and N. Braithwaite, *Physics of Radio-Frequency Plasmas* (Cambridge University Press, New York, 2011).
[22]T. Lafleur and P. Chabert, Plasma Sources Sci. Technol. **24**, 025017 (2015).
[23]S. I. Braginskii, *Reviews of Plasma Physics* (Consultants Bureau, New York, 1965), Vol. 1.
[24]F. F. Chen, I. D. Sudit, and M. Light, Plasma Sources Sci. Technol. **5**, 173 (1996).
[25]M. H. Lee and C. W. Chung, Phys. Plasmas **12**, 073501 (2005).
[26]J. G. Laframboise, "Theory of spherical and cylindrical Langmuir probes in a collisionless, Maxwellian plasma at rest," Technical Report No. 100, Institute for Aerospace Studies, University of Toronto, 1966.
[27]S. Chen and T. Sekiguchi, J. Appl. Phys. **36**(8), 2363 (1965).
[28]S. E. Koonin, *Computational Physics* (The Benjamin/Cummings Publishing Company, Inc., Menlo Park, California, 1986).